Atmos. Meas. Tech. Discuss., 8, 2521–2554, 2015
www.atmos-meas-tech-discuss.net/8/2521/2015/
doi:10.5194/amtd-8-2521-2015

Atmospheric Measurement Techniques Discussions
Open Access

MISR calibration issues in high-contrast scenes, and empirical corrections

J. A. Limbacher[1,2] and R. A. Kahn[1]

[1]Earth Science Division, NASA Goddard Space Flight Center, Greenbelt, MD 20771, USA
[2]Science Systems and Applications Inc., Lanham, MD 20706, USA

Received: 23 February 2015 – Accepted: 25 February 2015 – Published: 9 March 2015

Correspondence to: R. A. Kahn (ralph.kahn@nasa.gov)

Published by Copernicus Publications on behalf of the European Geosciences Union.

Abstract

We diagnose the potential causes for the Multi-angle Imaging SpectroRadiometer's (MISR) persistent high aerosol optical depth (AOD) bias at low AOD with the aid of coincident MODerate-resolution Imaging Spectroradiometer (MODIS) imagery from NASA's Terra satellite. Internal reflections within the MISR instrument are responsible for a large portion of the high AOD bias in high-contrast scenes, which are especially common as broken-cloud situations over ocean. Discrepancies between MODIS and MISR nadir-viewing near-infrared (NIR) images are used to optimize nine parameters, along with a background reflectance modulation term (that was modeled separately), to represent the observed features. Independent, surface-based AOD measurements from the AErosol RObotic NETwork (AERONET) and the Marine Aerosol Network (MAN) are compared with MISR Research Algorithm (RA) AOD retrievals for 1118 coincidences to validate the corrections when applied to the nadir and off-nadir cameras. Additionally, the calibration coefficients for the red and NIR channels used for MISR over-water aerosol retrievals were reassessed with the RA to be consistent on a camera-by-camera basis. With these corrections, plus the baseline RA corrections applied (except enhanced cloud screening), the median AOD bias in the mid-visible (green) band decreases from 0.010 to 0.002, the RMSE decreases by ∼ 10 %, and the slope and correlation of the MISR vs. sun photometer Ångström Exponent improves. For $AOD_{558\,nm} < 0.10$ and with additional cloud screening, the median bias for the RA-retrieved AOD in the green band decreases from 0.011 to 0.003, compared to ∼ 0.023 for the Standard Algorithm (SA). RMSE decreases by ∼ 20 % compared to the baseline (uncorrected) RA and by 17–53 % compared to the SA. After all corrections and cloud screening are implemented, for $AOD_{558\,nm} < 0.10$, which includes about half the validation data, 68 % absolute AOD errors for the RA have dropped to < 0.02 (∼ 0.018).

AMTD
8, 2521–2554, 2015

MISR calibration issues in high-contrast scenes

J. A. Limbacher and R. A. Kahn

1 Introduction

The Research Aerosol Retrieval algorithm (RA) for the NASA Earth Observing System's Multi-angle Imaging SpectroRadiometer (MISR) is used to analyze regional wildfire smoke, desert dust, urban pollution, volcanic ash, and other individual events, and to test algorithm modifications that might ultimately be applied to the MISR Standard Aerosol Retrieval algorithm (SA) that generates the operational product for the entire MISR data set (e.g., Kahn et al., 2001; Kahn and Limbacher, 2012; Limbacher and Kahn, 2014). The RA relies on the MISR standard Level 1B2 product for radiometrically and geometrically calibrated, spectral reflectance data as input for the aerosol retrievals. The spectral aerosol optical depth (AOD), retrieved over water using multi-angle data in the MISR red and near-infrared (NIR) bands, is sensitive to both the absolute reflectance and its spectral dependence, and retrieved aerosol type is even more sensitive to these values (Kahn and Gaitley, 2015). Although considerable effort has produced a MISR Level 1 product with about 3 % absolute radiometric accuracy, and generally even better band-to-band and camera-to-camera relative calibration (Bruegge et al., 2004, 2007; Diner et al., 2004; Kahn et al., 2005; Lyapustin et al., 2007; Lallart et al., 2008), there remain some artifacts in the radiometry that have not been characterized quantitatively (e.g., Bruegge et al., 2004). These can affect both the AOD (including a generally high mid-visible AOD bias of ~ 0.02 for low-AOD cases over dark water) and especially the aerosol type results (e.g., Kahn et al., 2010; Limbacher and Kahn, 2014).

In Limbacher and Kahn (2014), we showed that a small positive bias remained in the RA at low AOD over ocean (~ 0.01 for the green at AOD < 0.10), even with all the adjustments that were implemented in that study. In the current paper, we identify reflections within the instrument (primary and secondary mirroring convolved with background reflectance modulation, and blurring) as contributing to, and possibly accounting fully for, the observed bias. We use comparisons with (1) coincident observations by the MODerate-resolution Imaging Spectroradiometer (MODIS) that flies with

AMTD
8, 2521–2554, 2015

MISR aboard the NASA Earth Observing System's Terra satellite to develop empirical corrections to artifacts observed in the MISR/MODIS reflectance ratios in high-contrast scenes. Validation of the internal reflections corrections is performed using the MISR RA constrained by coincident measurements from (2) AErosol RObotic NETwork (AERONET) surface-based sun and sky scanning photometers (Holben et al., 1998), and (3) the associated Marine Aerosol Network (MAN) sun photometers (Smirnov et al., 2009), to identify and empirically adjust the MISR calibration coefficients to maximize camera-to-camera consistency.

2 Validation datasets and validation methodology

MODIS imagery allows for direct, radiometric comparison with observations from the MISR nadir-viewing camera only. Results for the full range of MISR cameras are validated to the extent possible by comparing the AOD derived from the MISR Research Aerosol Retrieval algorithm, using corrected radiometry, with coincident surface-based sun photometer values.

2.1 The MODIS dataset

MODIS radiometric calibration is based on a combination of on-board solar diffuser, direct space and lunar, and relatively unchanging desert-site observations, all modifying the pre-launch laboratory calibration (Xiong and Barnes, 2006). The most recent systematic refinement of MODIS calibration was performed by Sun et al. (2012), which they determine brings all the MODIS Terra reflective solar spectral bands within about 2 % accuracy at nadir. Lyapustin et al. (2014) used advanced vicarious calibration to identify further adjustments that amount to removing a trend of a few tenths-of-percent in the MODIS Terra calibration; this stabilizes the derived reflectance time-series for desert validation sites, and brings MODIS Terra radiometry into better agreement with that of its sister MODIS instrument that flies on the Aqua satellite.

AMTD
8, 2521–2554, 2015

Title Page
Abstract | Introduction
Conclusions | References
Tables | Figures
◀| |▶
◀ ▶
Back | Close
Full Screen / Esc
Printer-friendly Version
Interactive Discussion

To obtain the best available radiometric accuracy, we apply the Lyapustin et al. (2014) adjustments to the MODIS Collection 6 Level 1B, 1 km reflectance data when making comparisons with MISR. The MISR spectral bands are centered at 446 (blue), 558 (green), 672 (red), and 866 nm (NIR). MODIS bands closest to the MISR ones are band 4 (554 nm, green), and band 2 (856 nm, NIR). The MISR-MODIS comparisons in this study are performed for the spectral band that is closest and where the contrasts are greatest, i.e., over dark water scenes having well defined, bright ice patches in the NIR. MISR observations are coincident with MODIS Terra (hereafter just MODIS), and capture approximately ±190 km in the center of the 2300 km MODIS swath, so MODIS swath-edge and scan-angle issues are minimal or non-existent for the analysis performed here.

2.2 The MAN/AERONET dataset

Surface-based sun photometers provide ground-truth for satellite AOD retrieval validation (e.g., Kahn et al., 2010; Levy et al., 2014). The AERONET CIMEL instruments are calibrated periodically against standard instruments, and provide AOD measurement accuracy of approximately ±0.01 at ~ 550 nm wavelength (Eck et al., 1999). The hand-held MicroTops instruments used for MAN shipboard observations offer AOD accuracy of approximately ±0.02 (Smirnov et al., 2009). Ångström Exponents used for validation were calculated from the sun photometer AOD values by first interpolating to the four MISR effective wavelengths using linear interpolation in log space, and then finding the slope of the least-squares line fit to the interpolated AOD values also in log space, as we've done in previous studies. We obtained 178 near-coincident MAN and 940 AERONET, over-water or island observations to compare with AOD retrieved with the RA, using the re-calibrated MISR reflectances. Further description of the globally distributed, AERONET/MAN coincident data set used here is given in Limbacher and Kahn (2014).

2.3 The MISR research algorithm

Details of the MISR RA as applied in this paper can be found in Limbacher and Kahn (2014). Briefly, over water, the RA compares the MISR-observed equivalent reflectances with simulated top-of-atmosphere (TOA) values for a range of aerosol component and mixture optical models. All (aerosol-mixture/AOD) pairs that meet an adaptive χ^2 test criterion, that includes absolute and relative components, are considered adequate matches to the observations. The lower boundary condition in the simulations is represented as a black, Fresnel-reflecting ocean surface, with glitter masking and standard, wind-speed-related whitecap modeling, plus under-light due to near-surface dissolved organic matter and *chlorophyll a*. Where available, wind and ocean-color constraints were obtained from the daily Cross-Calibrated Multi-Platform (CCMP) (Atlas et al., 2011) and GlobColour (Barrot et al., 2010) products, respectively, and from climatology elsewhere. All the physical and empirical RA upgrades described in Limbacher and Kahn (2014) were applied where the RA is used, including the empirical radiometric adjustment to the red and NIR bands; nominal cloud screening from the MISR Standard algorithm is applied, but where noted below, we perform additional cloud screening based on the fraction not clear (FNC) in the coincident MODIS cloud-fraction product. For the purposes of the current paper, we refer to the RA including all these upgrades except the FNC adjustment as the "baseline" RA. The initial MISR-MODIS reflectance comparisons are performed with the standard MISR L1B2 data, with the appropriate out-of-band corrections applied.

2.4 MISR calibration approach

We studied the ratio of MISR to MODIS reflectances across the MISR nadir-camera swath as a means of identifying possible calibration anomalies. We rely on MODIS as the standard in this application, as MODIS is a scanning instrument whereas MISR is a push-broom imager, having fixed viewing optics that observes around the center of the MODIS swath. (As such, "ghosting" would show up along the spacecraft ground track for MODIS, and "latency" would operate across track. It is the opposite for MISR, making it possible to separate these issues. See below.) Ocean scenes partly filled with ice or very distinct clouds were selected (e.g., Figs. 1a, 2a, and 3a), to provide sharp brightness contrasts that can highlight artificial reflections and other imaging issues (e.g., Fig. 1a). We considered four possible sources of radiometry artifacts in the MISR data:

1. Internal Reflections – which include reflections from the camera optics into the detector. This would produce a pattern of reduced contrast in high-contrast scenes: brightening over darker regions and darkening over bright regions. The effect should be absent over uniformly bright or dark scenes, and would include both veiling light, which amounts to uniformly spread radiance over the detector, and "ghosting," which accounts for more structured reflectance features at the detector.

2. Latency – which amounts to pixels retaining signal from previous fields-of-view. For a given pixel, this would produce brightening as the detector moves from a bright to a dark target, and would be especially apparent when crossing a sharp edge, e.g., snow-covered land or sea-ice to dark ocean. The converse would occur moving from dark to bright targets, though the signal might be less apparent.

3. 3-D effects – which include side-scattering within the scene itself that is not accounted for in the interpretation of observed radiances. Such effects would stand out for scattered or broken cloud scenes, especially over dark water, and would not be as significant if the scene contrast is exclusively at the surface, such as some of the sea-ice scenes that are used for the current study. It would also be unlikely to mimic the geometry of the scene contrast features to the same degree as internal reflections.

4. Radiometric Calibration – which references the dependence of derived radiance on scene brightness; it might not be linear (as is assumed), particularly at very low

AMTD
8, 2521–2554, 2015

and/or very high scene brightness. For the nadir camera, comparison with MODIS Terra over bright and dark scenes would be a possible test, though differences between MISR and MODIS would not necessarily point to either instrument as the source of calibration error, except if an instrument shows long-term, systematic variations for a radiometrically stable target.

We began by converting the MISR Level 1B2 radiance data to equivalent reflectance, and applying the out-of-band corrections to the data (Chrien et al., 2001). Internal reflections and latency would affect the original MISR line-array detector pixels, whose output is recorded in the MISR Level 1B1 product. The MISR Level 1B2 pixel-level data are resampled from the original Level 1B1 data, taking account of geometric and radiometric calibration considerations (Bruegge et al., 1999; Jovanovic et al., 1999, 2002), and are used in the aerosol retrievals. As the L1B1 data is only archived for the most recent 90 days of acquisition, we first approximately undid the L1B2 geometric resampling by rotating the index matrices corresponding to the region of interest. The equations of rotation for a 2-D array are:

$$x' = x\cos(\theta) - y\sin(\theta)$$
$$y' = x\sin(\theta) + y\cos(\theta) \tag{1}$$

Here, x and y correspond to the x (along-track) and y (across-track) location index arrays. θ represents the rotation angle, and, because we use a left-hand coordinate system, a positive θ corresponds to clockwise rotation. The rotation is performed about the center pixel on each line separately, and varies based on latitude, camera, and sample. We adopted empirical values for the camera-by-camera angles of rotation (θ) that are determined with an optimization algorithm that matches the corresponding rotated L1B2 data to available L1B1 data. This algorithm first shrinks or expands the valid L1B2 data until it fits the L1B1 data, then proceeds to rotate the data by an angle which varies with latitude and by a fixed angle for each camera (for each of the right half and left half of the scenes), a process that corresponds to unwrapping the data from the ellipsoid (Earth) to which the L1B2 data are projected. The optimization routine maximizes the correlation between the L1B1 data and the new rotated dataset, for a validation set of L1B1 data to which we had access. This process yields both the latitudinally dependent angle correlating to the Earth's rotation, and the fixed angle required to unwrap the image from the ellipsoid. Figure 4 shows the optimized rotation angle as a function of latitude and sample along the focal plane line array, for each camera. Note the difference in the rotation angle between left and right halves of the swaths for the off-nadir cameras, representing the components of the rotations about the middle of the detector arrays. Ideally, the internal-reflection corrections should be implemented in the MISR Level 1 processing, to avoid these approximations and other limitations imposed when the data are first processed to Level 1B2, such as the L1B2 imagery being trimmed near the poles.

After rotation, the coincident MODIS-Terra reflectance data were re-gridded using a nearest-neighbor approach to match the rotated MISR reflectance data, so reflectance ratios and differences could be plotted (e.g., panels c and d of Figs. 1, 2 and 3) and analyzed. We determined radiometric corrections empirically, by iteratively testing and adjusting the coefficients of functions representing the observed anomaly patterns in the MISR reflectance images of high-contrast scenes using an optimization scheme, as described in the next section. A flow-chart of the entire calibration-adjustment-determination process is given in Fig. 5.

3 MISR calibration refinement

We identified specific patterns in the MISR/MODIS ratio images where MISR systematically overestimates the reflectance compared to MODIS. Examining pixel reflectance data where the MISR push-broom line arrays moved first over a bright, snow-cover surface and then across a sharp contrast transition to dark water, we found no evidence of latency effects. Similarly, other factors so dominate broken-cloud scenes that we did not observe any clear evidence for 3-D effects in the MISR imagery studied (although

AMTD
8, 2521–2554, 2015

such effects would affect MODIS as well as MISR, and therefore would not be present in the MISR/MODIS ratios anyway).

However, we identified four separate phenomena affecting the light impinging on MISR's focal plane that could be described as forms of internal reflection, plus a non-linear background variation in the MISR-MODIS reflectance ratio that appears to modulate the other reflectance anomalies. These are generally small effects, probably amounting to a few percent or less in many scenes globally, especially over land. But the effects can be much larger in high-contrast scenes, and even in less extreme situations, they can have a dominant impact on aerosol retrievals, particularly at low AOD over dark water, as we demonstrate below.

We model the first three effects and the associated background modulation, as these contributions are large enough to quantify empirically. The background modulation is modeled by hand from a few ideal scenes having relatively uniform clouds or ice features (Fig. 6). The fourth, uniform veiling-light, typically represents a very small fraction of the total anomaly signal (Figs. 1d, 2d, and 3d, blue outlines), too small to quantify numerically with our empirical approach. Our attempt to model veiling light as a term in the empirical optimization routine gave us values of essentially zero for the resulting veiling-light coefficient (analogous to C_1 in the Eq. 2 below). However, veiling-light is still corrected to some degree by the three separate correction models we implement.

The first effect is a mirroring of the image about a line drawn down the center of the scene (Figs. 1d, 2d, 3d, purple outlines). The following equation approximates the error due to this mirroring:

$$\text{Mirror}_1 = b_i \cdot C_1 \left(\rho_i - \frac{\sum\limits_{n=-r_1}^{r_1} \left(\rho_{i+n}^{\text{mirror}}\right) \{|n|+1\}^{-p_1}}{\sum\limits_{n=-r_1}^{r_1} \{|n|+1\}^{-p_1}} \right) \tag{2}$$

C_1 represents the mirror amplitude, ρ_i is the MISR-reported reflectance at pixel i in the camera line array, ρ_i^{mirror} is the MISR-reported reflectance at pixel *i*_mirror in the cam-

Discussion Paper | Discussion Paper | Discussion Paper | Discussion Paper |
AMTD
8, 2521–2554, 2015

era line array, r_1 gives the range of pixels over which the reflectance from pixel ρ_i makes mirroring contributions, p_1 provides distance-weighting, to account for decreasing contributions away from the mirroring peak, and b_i represents the background non-linear reflectance function, relative to MODIS, that we assume affects both the primary and secondary mirrors (Fig. 6). Because $\rho_i - \rho_i^{\text{mirror}}$ represents the contrast between the mirror pixel and the corresponding image pixel, the mirroring coefficient is multiplied by this difference on the RHS of Eq. (2) to produce an approximate contrast correction. The weighting includes $|n|$ so the contributions are symmetric about ρ_i, and 1 is added to avoid arbitrarily setting the mirror pixel reflectance to 0 at $n = 0$.

The background non-linear reflectance function was computed by identifying several scenes where nearly half the image appears homogeneous (and hence should produce a nearly constant mirroring correction if there were no background modulation). Once the scenes were identified, we normalized the MISR–MODIS reflectances by the minimum value of MISR–MODIS reflectance difference, and fit a function to the corresponding normalized differences by eye (Fig. 6). Figure 7, which presents 18 high-contrast images both before and after correction, illustrates how this background non-linear reflectance function contributes to reducing the reflectance anomalies.

The second effect is a secondary mirroring of the scene quarters, and there can be four of these mirrors (Figs. 1d, 2d, 3d, green outlines). The following equation approximates the error due to this secondary mirroring:

$$\text{Mirror}_2 = b_i \cdot C_2 \left(\rho_i^{\text{quarter}} - \frac{\sum_{n=-r_2}^{r_2} \left(\rho_{i+n}^{\text{quarter\_mirror}}\right) \{|n|+1\}^{-p_2}}{\sum_{n=-r_2}^{r_2} \{|n|+1\}^{-p_2}} \right) \quad (3)$$

C_2 is the secondary mirror amplitude, r_2 and p_2 define the range of pixels impacted and the distance weighting, respectively, and $\rho_i^{\text{quarter\_mirror}}$ is the MISR-reported reflectance at pixel *i*_quarter_mirror in the camera line array, evaluated by applying Mirror_2 across each half of each line of pixels separately (e.g., in a 200 pixel array, for *i*_quarter = 1, *i*_quarter_mirror would equal 100). As such, Mirror_2 correction terms extend into the quarter of the image being corrected.

We found it necessary to add a third effect that amounts to a blurring of the image, observed most readily along edges of high contrast, similar to a modified point spread function (Figs. 1d, 2d, 3d, brown outlines). The following equation approximates the error due to image blurring:

$$\text{Blur} = C_3 \left(\rho_i - \frac{\sum_{n=-r_3}^{r_3} (\rho_{i+n}) \{|n| + 1\}^{-p_3}}{\sum_{n=-r_3}^{r_3} \{|n| + 1\}^{-p_3}} \right) \tag{4}$$

where C_3 is the blur amplitude, and again, r_3 and p_3 define the range of pixels impacted and the distance weighting, respectively. The blur adjustment is applied over the entire image, but it has by far the biggest effect on scene elements having very high contrast, such as cloud and ice edges over dark water. We refer to the aggregate of these three as our empirical "ghosting" correction.

Before optimizing the parameters in Eqs. (2)–(4), we had to de-trend the MISR/MODIS reflectance ratios empirically, so the bright parts of the scenes retain a ratio of ∼ 1.0 from the beginning to the end of the mission. This required linearly increasing the MISR reflectance by 5 % from orbit 5000 to orbit 75 000. Further analysis of this aspect of the MISR calibration is beyond the scope of the current paper.

MISR internal reflection correction parameter optimization using MODIS

Eighteen high-contrast, low-AOD MISR and MODIS over-water scenes were used to optimize the nine "*C*," "*r*," and "*p*" parameters from Eqs. (3)–(5), as shown in Fig. 7a. (The "b_i" correction in Eqs. (2) and (3) is determined separately from the background MISR-MODIS reflectance ratio, as illustrated in Fig. 6.) The parameter optimization

AMTD
8, 2521–2554, 2015

is done only for the nadir camera NIR band, in part because we only have MODIS nadir-viewing data. Spectrally, the MISR and MODIS bands are most similar in the green and NIR channels, and the greatest relative errors requiring correction (and correspondingly, largest cost-function reductions) are found for scenes having low AOD and high contrast, which occur most frequently in the NIR band over water.

The method of optimization involves minimizing the following cost function:

$$\mathrm{Cost} = \frac{\sum_{i=0}^{n} \left| 1.0 - \frac{\mathrm{MISR_{new}}}{\mathrm{MODIS}} \right|}{n} \tag{5}$$

Here, $\mathrm{MISR_{new}}$ represents the corrected MISR pixel reflectance, MODIS is the nearest MODIS pixel reflectance, and n represents the number of data points used for the parameter optimization. We apply this cost function because it is not very sensitive to outliers (no squared quantities) that could be present (e.g., due to data collocation errors).

Because we perform the optimization using several hundred thousand data points, it would be too computationally time consuming to treat all nine parameters simultaneously. We instead optimize the three primary mirroring parameters (Eq. 2) first. This is done using only the portion of the scene where the primary mirroring clearly occurs (i.e., bright regions reflected across the image centerline, such as the purple outlines in Figs. 1d, 2d, and 3d). We also mask any places where the MODIS data is greater than 5 times the fifth percentile value for the aggregated MODIS reflectance data, to avoid the brighter cloud or ice-covered regions, where geo-location error can create large apparent reflectance anomalies; this specific criterion was determined empirically. A resulting C_1 of 0.01, a p_1 of 0.60, and a r_1 of 155 decrease our cost function (Eq. 5) by 77 % compared to the control value, based on primary mirroring and 648 685 data points (the dark side half of each of the scenes in Fig. 7).

We then optimize the remaining six parameters simultaneously using the other half of the scene (where the primary mirroring does not occur), while also masking any data where the MODIS data is greater than 5 times the fifth percentile value for the MODIS reflectance data. An optimized C_2 of 0.006, a p_2 of 0.05, a r_2 of 180 (this is the entire half of the image), a C_3 of 0.0375, a p_3 of 1.70, and a r_3 of 85, result in a 46 % reduction of our cost function (Eq. 5) compared to the control value, based on secondary mirroring, blurring correction, and 337 524 data points in the second half of the image (the bright half of each of the scenes in Fig. 7). Note that segmenting the image is required only when deriving the nine correction parameters; once determined, the corrections are applied over entire images. Taken together, all nine parameters reduce the cost function by 68 % for the 993 473 data points that are not masked over the entire scene. We validate these results in the next section.

4 Combined correction and validation using the MISR research algorithm

Unlike MODIS, MISR has multiple view angles, and the spectral responses of the two instruments are not identical, so we require a different way to validate the 35 MISR channels other than the nadir NIR. We attempted to use forward model radiative transfer results computed from the MISR/MAN coincidences to compare with the TOA reflectances from MISR (e.g., Kahn et al., 2005). However, the uncertainties in the forward model for each channel separately can be larger than the error due to internal reflections, which brings into question our ability to validate the nine coefficients separately for each channel. Instead, we (1) apply the nadir NIR internal reflection corrections to the MISR TOA reflectances for all 36 channels, under the assumption that the effects are dominated by similarities in the optics geometry of the different cameras, (2) run the RA with all the adjustments made in Limbacher and Kahn (2014) on the corrected reflectances, both with and without the enhanced cloud screening, and (3) compare the RA-retrieved AODs and Ångström Exponents (ANGs) with results from coincident MAN/AERONET observations for validation, and with the corresponding Standard Algorithm (SA) retrievals. We modified the acceptance criterion at low AOD from that used in Limbacher and Kahn (2014) as a result of the corrections that

AMTD
8, 2521–2554, 2015

are applied to the TOA reflectances. We select all mixtures falling within the minimum χ^2 value + 0.75 at low AOD, rather than the minimum χ^2 value + 0.35, after the corrections are applied. This avoids artificially constraining aerosol type at low AOD; the need occurs because the denominator of the χ^2 variable, that represents the measurement uncertainty, decreases due to the corrections (see Limbacher and Kahn, 2014).

4.1 Modifications to uncertainty envelopes, and calibration adjustments

Because the fraction of data falling below a given error criterion is highly dependent on retrieved AOD, we modified the "uncertainty envelopes" used to report agreement with validation data from those of previous MISR validation papers. Specifically, we find the size of the envelope so ~ 68 % of the data falls within it at all AODs. We divided the AOD results into 50 bins, with equal numbers of points in each bin, and determined the 68 % absolute errors corresponding to each AOD bin. Then a regression line was fit to the 68 % errors, and slope and intercept values were derived. The resulting AOD uncertainty envelope for the validation data set used here is:

$$\mathrm{AOD_{unc}} = \pm(0.10 \cdot \mathrm{AOD_{spectral}} + 0.013) \quad (6)$$

where $\mathrm{AOD_{spectral}}$ is the AOD reported at any of the four wavelengths. The coefficients of this envelope do not vary substantially with wavelength. Also, we find that representing the ANG uncertainty as:

$$\mathrm{ANG_{unc}} = \pm(e^{-25 \cdot \mathrm{AOD_{Green}}} + 0.15) \quad (7)$$

results in about 68 % of the ANG data falling within this uncertainty metric over the entire range of AOD. Note that this function represents the exponentially increasing MISR sensitivity to particle microphysical properties with increasing AOD (Kahn and Gaitley, 2015).

In our previous work, overall image empirical radiometric calibration coefficients of 1.0075 for the red and 0.9925 for the NIR were applied to the MISR reflectance data

AMTD
8, 2521–2554, 2015

to bring ANG into better alignment with coincident MAN/AERONET validation data (Limbacher and Kahn, 2014). Here, we refine those coefficients to give a more consistent camera-to-camera result. Using the MAN/AERONET validation dataset to select $AOD_{558\,nm} > 0.20$ cases, and MISR to constrain fraction not clear (FNC) < 0.50, in Fig. 8 we show the camera-by-camera coefficients necessary to bring the median $\rho - \rho_{model}$ residuals to zero for both the red and NIR bands, where ρ is the MISR reflectance, and ρ_{model} is the corresponding mean simulated reflectance of all passing mixtures. Note that these coefficients are not "true" calibration corrections (although for simplicity we may refer to them elsewhere in this paper as calibration coefficients), as we are using the MISR RA retrieval to create a self-consistent camera-to-camera result, rather than AERONET to constrain the aerosol type (mixture) and amount (AOD) for the forward model in this case. That is, the RA was run, and the modeled reflectances corresponding to the passing aerosol mixtures (and AODs) were averaged to produce ρ_{model}. The adjustments for the nadir NIR and red bands are consistent with earlier work by Kahn et al. (2005), which did use coincident AERONET constraints in the forward radiative transfer model, but limitations with the forward model and an imperfect aerosol mixture optical model list might also contribute to the observed discrepancies. Because these adjustments replace the coefficients in Limbacher and Kahn (2014), they are applied along with the internal reflection (ghosting) corrections, but are not applied to the baseline RA.

4.2 Validation against coincident AERONET and MAN data

Table 1 shows the statistics of ANG and AOD for low-AOD cases: AERONET/$MAN_{mid\text{-}vis}$ $AOD < 0.10$. Compared to both the SA and the RA without the internal reflection corrections implemented, the upgraded RA shows substantial improvement, both with and without enhanced cloud screening, for every AOD statistic considered. With enhanced cloud screening, the upgraded RA reports a median mid-visible AOD bias of only 0.003, compared to 0.023 for the SA, and 0.011 for the baseline RA. RMSE for the upgraded RA decreases by ~20 % compared to the baseline algorithm, and by 17–53 % compared to the SA. Median absolute error (MAE) for the upgraded RA decreases by 19–29 % compared to the baseline algorithm, and by 29–62 % compared to the SA.

Figure 9 shows the AOD and ANG results of the internal reflection correction (blue whiskers) compared to the baseline RA (green whiskers), and the SA (red whiskers), as a function of mid-visible AERONET AOD, when enhanced cloud screening is not applied. Note that the internal reflection corrections improve the results substantially for the lowest AOD bins, but have a smaller relative impact at higher AOD, as might be expected. Although the RA performs better statistically at high AOD compared to the SA, it is important to point out that the RA is also biased low in the blue and green bands at high AOD. This is likely due to a combination of: lack of quantitative sensitivity to SSA, a sparse mixture grid in the algorithm climatology (lacking many absorbing mixture options), and underlying calibration issues that would tend to show up at higher AOD (Kahn et al., 2010). The statistics of the data are given in Table 2, aggregated over all AOD. For the case of no additional cloud screening, the fraction of AOD data meeting our 1-sigma error envelope increases by about 0.06–0.08 for all wavelengths compared to the baseline RA and by 0.12–0.31 compared to the SA. The median spectral bias decreases from 0.010 for the baseline RA (and 0.01–0.04 for the SA) to < 0.005, and RMSE decreases by ~ 10 % compared to the baseline RA and 22–41 % compared to the SA. ANG improves only for the lowest AOD bins in Fig. 9, Row 5, but there is also an improvement in the ANG slope, increasing by about 0.05 for all AODs (not shown).

Figure 10 shows the AOD and ANG results similar to Fig. 9, but with the addition of enhanced cloud screening – a maximum FNC of 0.50. As Fig. 10 demonstrates, the AOD statistics improve for virtually every wavelength and AOD bin with this modification. Interestingly, unlike AOD, ANG seems to improve only in several of the lowest AOD bins. This could be due to the fact that as AOD increases, ANG becomes much more robust to small AOD changes, or to limitations of the aerosol optical model climatology used, and there might be some remaining band-to-band calibration issues, to which ANG is especially sensitive. Table 2 shows that the bias in AOD is now ≤ 0.002 for all wavelengths, and the bias in ANG aggregated over all AOD is also very small (< 0.025). Statistically, the SA, the baseline RA, and the RA with the internal-reflection corrections, all improve with additional cloud screening. However, the improvement is much greater for the baseline RA and especially the SA. This is primarily because the scenes containing the same objects that cause enhanced internal reflections, mainly bright clouds and sea ice over dark water, tend to be removed as the maximum allowed FNC is reduced.

5 Conclusions

In Limbacher and Kahn (2014), we showed that a small positive bias remained in the RA at low AOD over ocean (~ 0.01 for the green at AOD < 0.10), even with all the adjustments that were implemented in that study. We identify here the following internal reflections as contributing to, and possibly accounting fully for, the observed bias in TOA reflectance in high-contrast scenes that produces the AOD overestimation: primary and secondary mirroring convolved with background reflectance modulation, blurring, and possibly a small, uniform veiling-light. We developed relationships to represent the mirroring and blurring phenomena empirically, and optimized the corresponding parameters for the MISR nadir-camera NIR spectral band, using coincident MODIS NIR imagery.

MODIS does not provide corresponding data for independently testing the other eight cameras or the other nadir-camera spectral channels. So we applied the nadir NIR corrections to the other channels under the assumption that the effects are dominated by similarities in the optics geometry of the different cameras, and tested the results by comparing sun photometer validation data against AOD and ANG retrieved by the MISR Research Algorithm under this assumption. Compared to the RA without the internal-reflection corrections and to the SA, the corrections substantially improve spectral AOD agreement with the 1118 MAN/AERONET coincidences used for this study. For MAN/AERONET $AOD_{558\,nm} < 0.10$, 558 nm 68 % AOD errors decrease by 23 % compared to the RA and 50 % compared to the SA, when we impose a maximum fraction not clear (FNC) of 0.50 as additional cloud masking. With all these corrections implemented, for $AOD_{558\,nm} < 0.10$, 68 % AOD errors for all spectral bands fall under 0.020.

The results presented here show that with our Limbacher and Kahn (2014) algorithm upgrades, a maximum fraction not clear (FNC) of 0.50, and the internal-reflection corrections, the AOD bias at low optical depth over ocean is reduced to ≤ 0.003. In addition, these corrections bring the MISR nadir-camera NIR reflectance into much better agreement with MODIS band 2. Ideally, the internal-reflection corrections should be implemented in the MISR Level 1 processing, to avoid the image-rotation complications discussed in Sect. 2.4, as well as the image trimming effects that are noticeable near the poles. Further analysis and possible refinement of the MISR absolute and channel-to-channel calibration, and their variation over the MISR mission, are part of continuing work by the MISR calibration team (C. Bruegge, personal communication, 2014).

Acknowledgements. We thank our colleagues on the Jet Propulsion Laboratory's MISR instrument team and at the NASA Langley Research Center's Atmospheric Sciences Data Center for their roles in producing the MISR Standard data sets, as well as our colleagues on the MODIS team, Brent Holben and the AERONET team, and Alexander Smirnov and the MAN team for the invaluable data sets they produce. We also thank Sergey Korkin and Andrew Sayer for helpful discussions, Alexei Lyapustin for providing his MODIS radiometric correction code, Maksym Petrenko for identifying the MISR/MAN coincidences, and Carol Bruegge, James Butler, Veljko Jovanovic, and Michael Garay for comments on an early version of the manuscript. This research is supported in part by NASA's Climate and Radiation Research and Analysis Program under H. Maring, NASA's Atmospheric Composition Program under R. Eckman, and the NASA Earth Observing System MISR instrument project.

AMTD
8, 2521–2554, 2015

References

Atlas, R., Hoffman, R. N., Ardizzone, J., Leidner, S. M., Jusem, J. C., Smith, D. K., and Gombos, D.: A cross-calibrated, multiplatform ocean surface wind velocity product for meteorological and oceanographic applications, B. Am. Meteorol. Soc., 92, 157–174, doi:10.1175/2010BAMS2946.1, 2011.

Barrot, G., Mangin, A., and Pinnock, S.: GlobColour Product User Guide, available at: http://www.globcolour.info (last access: 31 January 2014), 2010.

Bruegge, C. J., Diner, D. J., Korechoff, R. P., and Lee, M.: MISR Level 1 Radiance Scaling and Conditioning Algorithm Theoretical Basis, Jet Propulsion Laboratory JPL D-11507, Rev E, available at: http://eospso.gsfc.nasa.gov/sites/default/files/atbd/atbd-misr-02.pdf (last access: 11 July 2014), 1999.

Bruegge, C. J., Abdou, W. A., Diner, D. J., Gaitley, B. J., Helmlinger, M. C., Kahn, R. A., and Martonchik, J. V.: Validating the MISR radiometric scale for the ocean aerosol science communities, in: Post-Launch Calibration of Satellite Sensors, edited by: Morain, S. A. and Budge, A. M., A. A. Balkema Publishers, Leiden, the Netherlands, 103–115, 2004.

Bruegge, C. J., Diner, D. J., Kahn, R. A., Chrien, N., Helmlinger, M. C., Gaitley, B. J., and Abdou, W. A.: The MISR radiometric calibration process, Remote Sens. Environ., 107, 2–11, doi:10.1016/j.rse.2006.07.024, 2007.

Bruegge, C. J., Diner, D. J., Gray, E., Jovanovic, V., Gray, E., Di Girolamo, L., and Zhao, G.: Radiometric stability of the Multi-angle Imaging SpectroRadiometer (MISR) following 15 years on-orbit, Proc. SPIE, 9218, doi:10.1117/12.2062319, 2014.

Chrien, N. L., Bruegge, C. J., and Gaitley, B. J.: AirMISR laboratory calibration and in-flight performance results, Remote Sens. Environ., 77, 328–337, 2001.

Diner, D. J., Kahn, R. A., Bruegge, C. J., Martonchik, J. V., Abdou, W. A., Gaitley, B. J., Helmlinger, M. C., Kalashnikova, O. V., and Li, W.-H.: Refinements to MISR's radiometric calibration and implications for establishing a climate-quality aerosol observing system, SPIE Proc., 5652, 57–65, 2004.

Diner, D. J., Abdou, W. A., Ackerman, T. P., Crean, K., Gordon, H. R., Kahn, R. A., Martonchik, J. V., McMuldroch, S., Paradise, S. R., Pinty, B., Verstraete, M. M., Wang, M., and West, R. A.: Multi-Angle Imaging SpectroRadiometer Level 2 Aerosol Retrieval Algorithm Theoretical Basis, Revision G, JPL D-11400, Jet Propulsion Laboratory, California Institute of Technology, Pasadena, 2008.

AMTD
8, 2521–2554, 2015

MISR calibration issues in high-contrast scenes

J. A. Limbacher and R. A. Kahn

Holben, B. N., Eck, T. F., Slutsker, I., Tanre, D., Buis, J. P., Sezter, A., Vermote, E., Reagan, J. A., Kaufman, Y. J., Nakajima, T., Lavenu, F., Jankowiak, I., and Smirnov, A.: AERONET – a federated instrument network and data archive for aerosol characterization, Remote Sens. Environ., 66, 1–16, 1998.

Jovanovic, V. M., Lewicki, S. A., Smyth, M. M., Zong, J., and Korechoff, R. P.: MISR Level 1 Georectification and Registration Algorithm Theoretical Basis, Jet Propulsion Laboratory JPL D-11532, Rev D, available at: http://eospso.gsfc.nasa.gov/sites/default/files/atbd/atbd-misr-03.pdf (last access: 11 July 2014), 1999.

Jovanovic, V. M., Bull, M. A., Smyth, M. M., and Zong, J.: MISR In-flight camera geometric model calibration and georectification performance, IEEE T. Geosci. Remote, 40, 1512–1519, 2002.

Kahn, R., Li, W.-H., Martonchik, J., Bruegge, C., Diner, D., Gaitley, B., Abdou, W., Dubovik, O., Holben, B., Smirnov, S., Jin, Z., and Clark, D.: MISR low-light-level calibration, and implications for aerosol retrieval over dark water, J. Atmos. Sci., 62, 1032–1062, 2005.

Kahn, R. A. and Gaitley, B. J.: An analysis of aerosol type as retrieved by MISR, J. Geophys. Res., submitted, 2015.

Kahn, R. A. and Limbacher, J.: Eyjafjallajökull volcano plume particle-type characterization from space-based multi-angle imaging, Atmos. Chem. Phys., 12, 9459–9477, doi:10.5194/acp-12-9459-2012, 2012.

Kahn, R. A., Banerjee, P., and McDonald, D.: The sensitivity of multiangle imaging to natural mixtures of aerosols over ocean, J. Geophys. Res., 106, 18219–18238, 2001.

Kahn, R. A., Gaitley, B. J., Garay, M. J., Diner, D. J., Eck, T., Smirnov, A., and Holben, B. N.: Multiangle imaging spectroradiometer global aerosol product assessment by comparison with the Aerosol Robotic Network, J. Geophys. Res., 115, D23209, doi:10.1029/2010JD014601, 2010.

Lallart, P., Kahn, R. A., and Tanré, D.: POLDER2/ADEOSII, MISR, and MODIS/Terra reflectance comparisons, J. Geophys. Res., 113, D14S02, doi:10.1029/2007JD009656, 2008.

Levy, R. C., Mattoo, S., Munchak, L. A., Remer, L. A., Sayer, A. M., Patadia, F., and Hsu, N. C.: The Collection 6 MODIS aerosol products over land and ocean, Atmos. Meas. Tech., 6, 2989–3034, doi:10.5194/amt-6-2989-2013, 2013.

Limbacher, J. A. and Kahn, R. A.: MISR research-aerosol-algorithm refinements for dark water retrievals, Atmos. Meas. Tech., 7, 3989–4007, doi:10.5194/amt-7-3989-2014, 2014.

AMTD
8, 2521–2554, 2015

MISR calibration issues in high-contrast scenes

J. A. Limbacher and R. A. Kahn

Lyapustin, A., Wang, Y., Kahn, R., Xiong, J., Ignatov, A., Wolfe, R., Wu, A., Holben, B., and Bruegge, C.: Analysis of MODIS-MISR calibration differences using surface albedo around AERONET sites and cloud reflectance, Remote Sens. Environ., 107, 12–21, doi:10.1016/j.rse.2006.09.028, 2007.

Lyapustin, A., Wang, Y., Xiong, X., Meister, G., Platnick, S., Levy, R., Franz, B., Korkin, S., Hilker, T., Tucker, J., Hall, F., Sellers, P., Wu, A., and Angal, A.: Scientific impact of MODIS C5 calibration degradation and C6+ improvements, Atmos. Meas. Tech., 7, 4353–4365, doi:10.5194/amt-7-4353-2014, 2014.

Smirnov, A., Holben, B. N., Slutsker, I., Giles, D. M., McClain, C. R., Eck, T. F., Sakerin, S. M., Macke, A., Croot, P., Zibordi, G., Quinn, P. K., Sciare, J., Kinne, S., Harvey, M., Smyth, T. J., Piketh, S., Zielinski, T., Proshutinsky, A., Goes, J. I., Nelson, N. B., Larouche, P., Radionov, V. F., Goloub, P., Krishna Moorthy, K., Matarrese, R., Robertson, E. J., and Jourdin, F.: Maritime Aerosol Network as a component of Aerosol Robotic Network, J. Geophys. Res., 114, D06204, doi:10.1029/2008JD011257, 2009.

Sun, J., Angal, A., Xiong, X.-J., Chen, H., Geng, X., Wu, A., Choi, T.-J., and Chu, M.: MODIS reflective solar bands calibration improvements in collection 6, Proc. SPIE, Vol. 8510, 85100J-1, doi:10.1117/12.930021, 2012.

Xiong, X.-J. and Barnes, W. L.: An overview of MODIS radiometric calibration and characterization, Adv. Atmos. Sci., 23, 69–79, 2006.

AMTD

8, 2521–2554, 2015

MISR calibration issues in high-contrast scenes

J. A. Limbacher and R. A. Kahn

Table 1. Statistics of AOD and ANG retrievals for AERONET/MAN mid-visible AOD < 0.10*.

Adjustment (Blue)	1 sigma (%)	2 sigma (%)	68	RMSE	MAE	Med Bias	#
SA	21	50	0.053	0.059	0.039	0.039	593
SA + 0.5 FNC	28	57	0.047	0.049	0.034	0.033	524
RA	52	81	0.029	0.036	0.019	0.016	593
RA + 0.5 FNC	62	88	0.023	0.028	0.016	0.011	524
RA + Ghost	63	88	0.023	0.029	0.015	0.008	593
RA + Ghost + 0.5 FNC	70	93	0.019	0.023	0.013	0.003	524
Adjustment (Green)	1 sigma	2 sigma	68	RMSE	MAE	Med Bias	#
SA	32	66	0.039	0.046	0.028	0.028	593
SA + 0.5 FNC	40	73	0.034	0.037	0.024	0.023	524
RA	55	83	0.026	0.033	0.018	0.015	593
RA + 0.5 FNC	62	89	0.022	0.026	0.014	0.011	524
RA + Ghost	67	90	0.020	0.027	0.013	0.007	593
RA + Ghost + 0.5 FNC	72	94	0.017	0.021	0.011	0.003	524
Adjustment (Red)	1 sigma	2 sigma	68	RMSE	MAE	Med Bias	#
SA	43	73	0.031	0.038	0.021	0.021	593
SA + 0.5 FNC	51	81	0.026	0.029	0.018	0.016	524
RA	55	83	0.025	0.032	0.017	0.015	593
RA + 0.5 FNC	63	90	0.021	0.025	0.014	0.010	524
RA + Ghost	67	91	0.019	0.025	0.012	0.006	593
RA + Ghost + 0.5 FNC	73	95	0.017	0.020	0.010	0.003	524
Adjustment (NIR)	1 sigma	2 sigma	68	RMSE	MAE	Med Bias	#
SA	53	82	0.024	0.030	0.016	0.013	593
SA + 0.5 FNC	60	88	0.021	0.023	0.014	0.008	524
RA	56	83	0.023	0.030	0.016	0.013	593
RA + 0.5 FNC	62	88	0.020	0.024	0.013	0.008	524
RA + Ghost	68	92	0.018	0.023	0.011	0.004	593
RA + Ghost + 0.5 FNC	72	95	0.016	0.019	0.010	0.002	524
Adjustment (ANG)	1 sigma	2 sigma	68	RMSE	MAE	Med Bias	#
SA	52	86	0.500	0.551	0.347	0.300	593
SA + 0.5 FNC	50	84	0.519	0.554	0.371	0.335	524
RA	73	93	0.340	0.457	0.220	-0.042	593
RA + 0.5 FNC	72	94	0.357	0.432	0.238	-0.052	524
RA + Ghost	75	95	0.321	0.434	0.205	0.012	593
RA + Ghost + 0.5 FNC	74	95	0.333	0.406	0.218	0.013	524

* Columns 2 and 3 give the percent of validation cases within the confidence envelopes indicated. Column 4 gives the RMSE is the root-mean-square error, MAE is the mean absolute error, Med Bias is the median bias, and # is the number of validation cases included. The first four data blocks give the spectral AOD statistics, and the fifth data block presents the ANG statistics.

AMTD
8, 2521–2554, 2015

MISR calibration issues in high-contrast scenes

J. A. Limbacher and R. A. Kahn

Table 2. Statistics of AOD and ANG retrievals for all AOD*.

Adjustment (Blue)	1 sigma (%)	2 sigma (%)	68	RMSE	MAE	Med Bias	#
SA	31	60	0.061	0.073	0.042	0.038	1118
SA + 0.5 FNC	36	65	0.054	0.065	0.036	0.032	977
RA	56	84	0.037	0.047	0.024	0.010	1118
RA + 0.5 FNC	62	88	0.034	0.044	0.021	0.005	977
RA + Ghost	62	89	0.032	0.043	0.021	0.002	1118
RA + Ghost + 0.5 FNC	65	91	0.030	0.042	0.019	−0.002	977
Adjustment (Green)	1 sigma	2 sigma	68	RMSE	MAE	Med Bias	#
SA	42	72	0.044	0.056	0.030	0.026	1118
SA + 0.5 FNC	48	77	0.038	0.048	0.025	0.020	977
RA	60	86	0.031	0.041	0.021	0.010	1118
RA + 0.5 FNC	65	91	0.027	0.037	0.018	0.006	977
RA + Ghost	67	91	0.027	0.037	0.018	0.002	1118
RA + Ghost + 0.5 FNC	69	93	0.026	0.034	0.016	−0.001	977
Adjustment (Red)	1 sigma	2 sigma	68	RMSE	MAE	Med Bias	#
SA	50	78	0.037	0.047	0.023	0.019	1118
SA + 0.5 FNC	58	84	0.030	0.039	0.020	0.012	977
RA	60	87	0.028	0.037	0.019	0.010	1118
RA + 0.5 FNC	66	91	0.025	0.032	0.016	0.006	977
RA + Ghost	68	91	0.024	0.033	0.017	0.003	1118
RA + Ghost + 0.5 FNC	72	94	0.023	0.030	0.015	0.000	977
Adjustment (NIR)	1 sigma	2 sigma	68	RMSE	MAE	Med Bias	#
SA	56	84	0.029	0.040	0.019	0.013	1118
SA + 0.5 FNC	63	90	0.025	0.033	0.016	0.007	977
RA	60	86	0.026	0.035	0.018	0.011	1118
RA + 0.5 FNC	66	90	0.024	0.029	0.016	0.005	977
RA + Ghost	68	91	0.022	0.031	0.015	0.004	1118
RA + Ghost + 0.5 FNC	72	94	0.021	0.027	0.014	0.000	977
Adjustment (ANG)	1 sigma	2 sigma	68	RMSE	MAE	Med Bias	#
SA	47	80	0.398	0.455	0.280	0.216	1118
SA + 0.5 FNC	46	79	0.425	0.463	0.296	0.236	977
RA	66	89	0.275	0.373	0.173	−0.042	1118
RA + 0.5 FNC	66	89	0.282	0.360	0.181	−0.038	977
RA + Ghost	69	91	0.247	0.354	0.159	−0.027	1118
RA + Ghost + 0.5 FNC	68	91	0.262	0.339	0.167	−0.022	977

* Columns 2 and 3 give the percent of validation cases within the confidence envelopes indicated, RMSE is the root-mean-square error, MAE is the mean absolute error, Med Bias is the median bias, and # is the number of validation cases included. The first four data blocks give the spectral AOD statistics, and the fifth data block presents the ANG statistics.

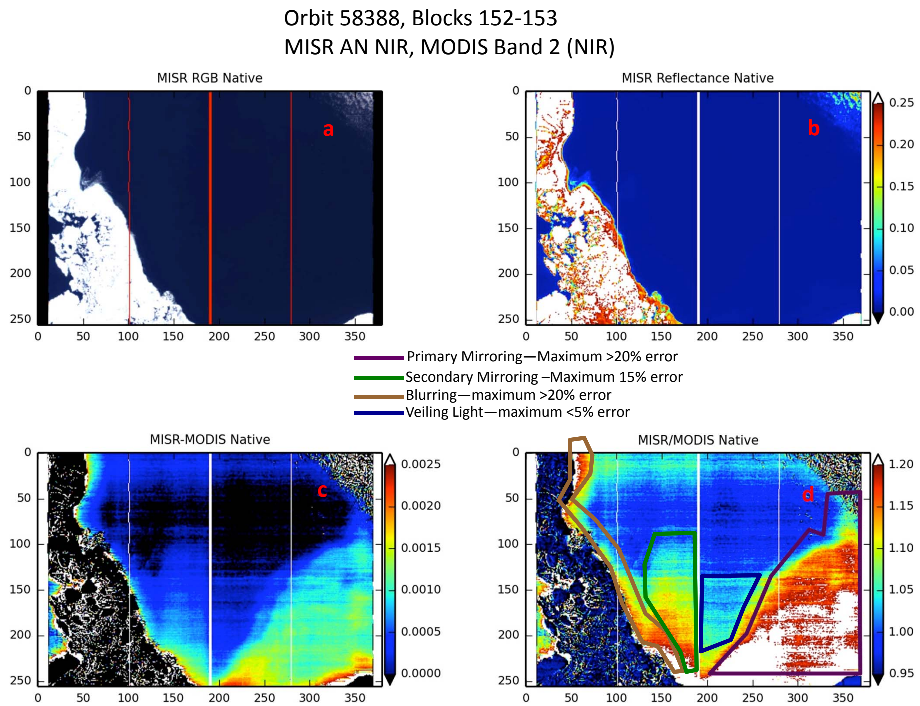

Figure 1. (a) MISR nadir-view (AN) RGB reflectance context image of an ice-and-dark-water scene. **(b)** MISR AN NIR reflectance for the scene. (Reflectance scale to the right of the image.) **(c)** MISR (AN NIR)–MODIS (NIR) reflectance differences. (Difference scale to the right of the image.) **(d)** MISR (AN NIR)/MODIS (NIR) ratios for the scene. The four contours in this panel outline approximately the areas where optical anomalies occur (color key in the middle of the figure). The image presented corresponds to MISR orbit 58 388, blocks 152–153. The vertical lines stretching down the images represent the 25, 50 and 75 % of the image that contains valid data. Native refers to the fact that the MISR data have been rotated to its native (L1B1) format.

AMTD
8, 2521–2554, 2015

MISR calibration issues in high-contrast scenes

J. A. Limbacher and R. A. Kahn

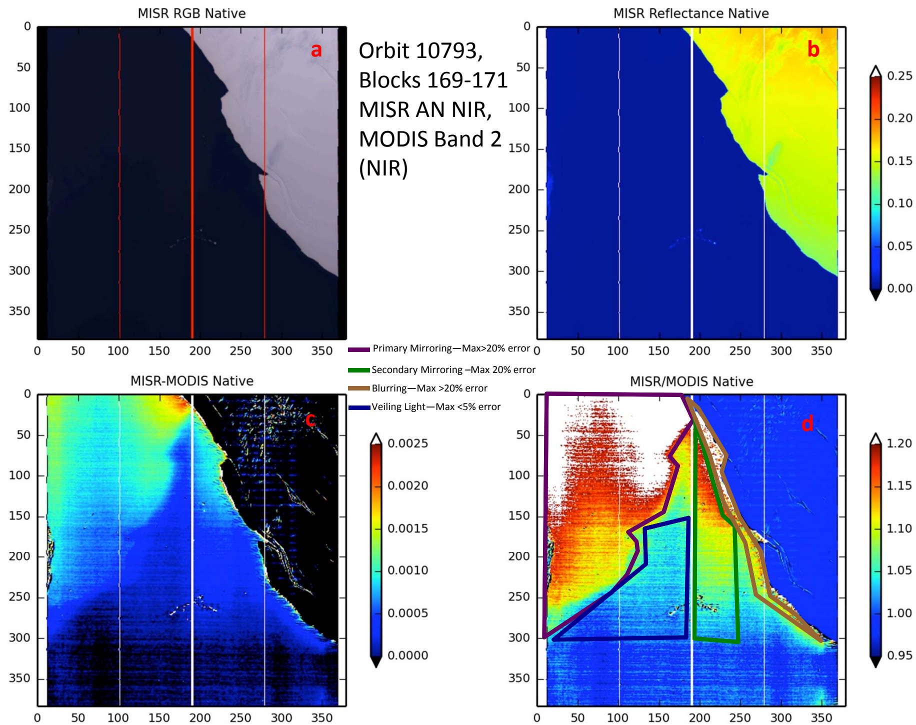

Figure 2. Same as Fig. 1, but for MISR orbit 10 793, blocks 169–171.

AMTD
8, 2521–2554, 2015

MISR calibration issues in high-contrast scenes

J. A. Limbacher and R. A. Kahn

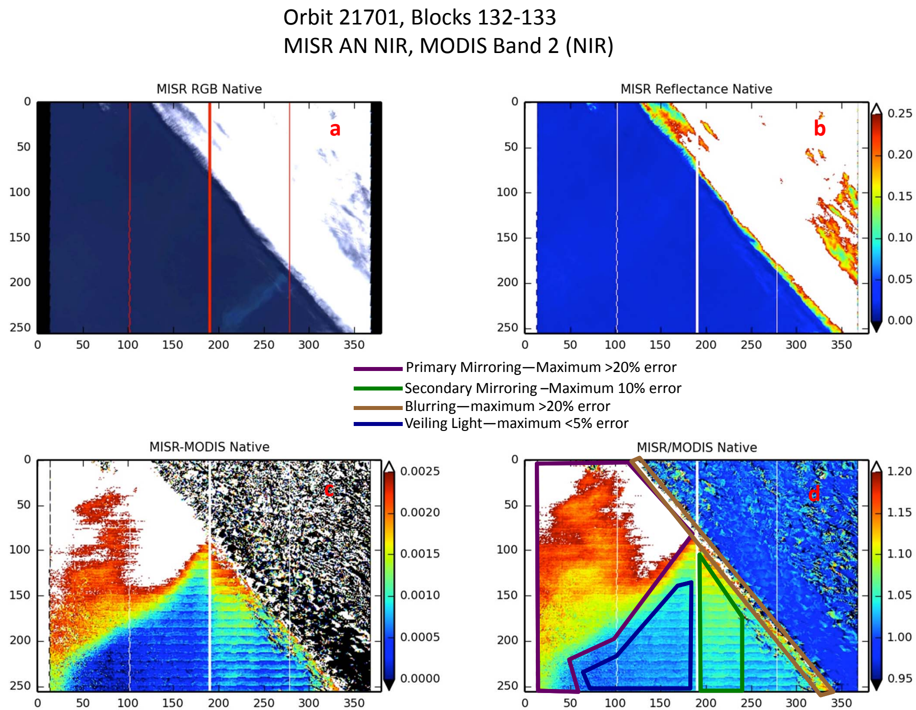

Figure 3. Same as Fig. 1, but for MISR orbit 21 701, blocks 132–133.

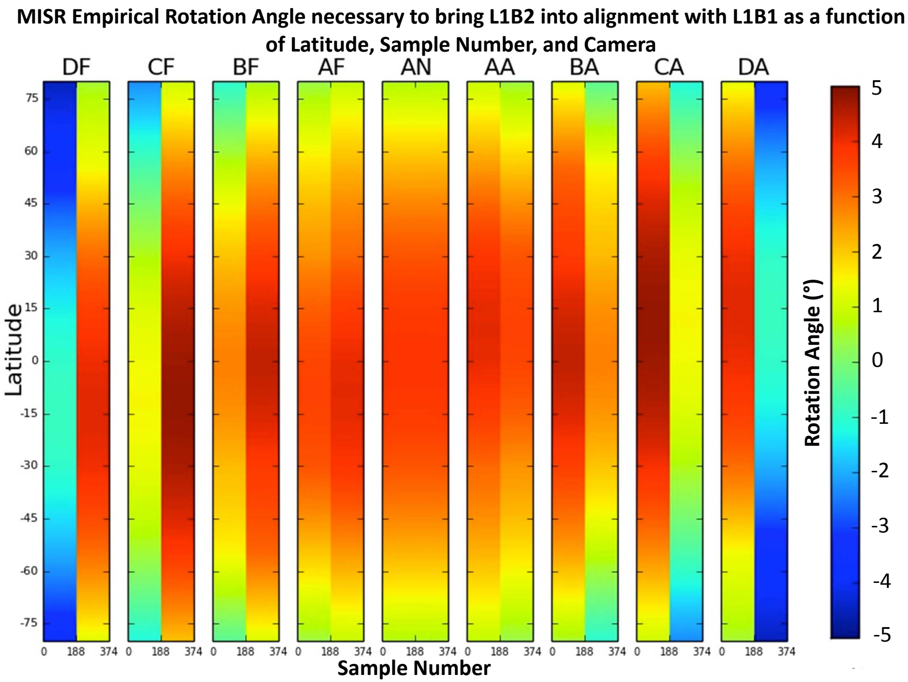

Figure 4. These nine plots represent the empirically derived rotation angles used to bring MISR L1B2 data into agreement with MISR L1B1 data, as a function of Latitude and MISR sample number along the focal plane line array, for each camera. Because these angles were calculated empirically using an optimization routine, the rotation angles are approximate.

AMTD
8, 2521–2554, 2015

MISR calibration issues in high-contrast scenes

J. A. Limbacher and R. A. Kahn

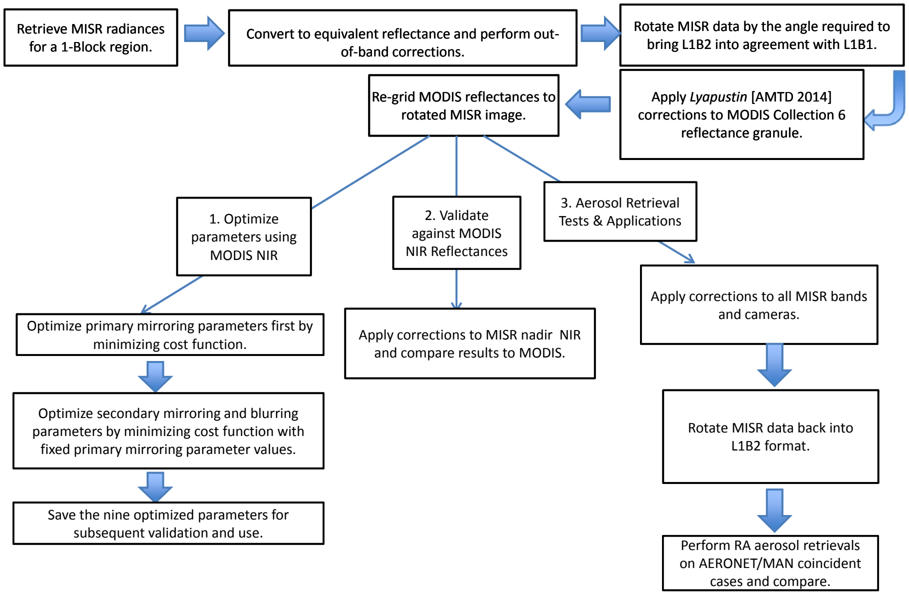

Figure 5. Flow-chart summarizing the steps involved in the MISR internal reflection correction.

AMTD
8, 2521–2554, 2015

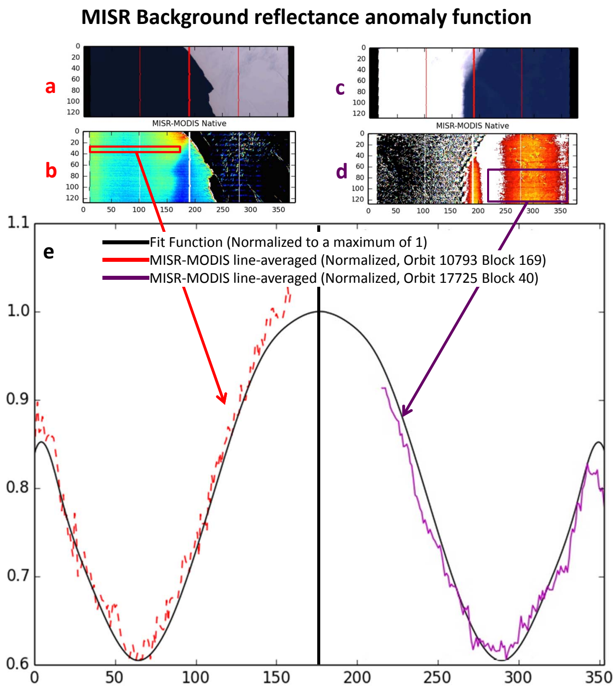

Figure 6. (a) MISR RGB image for orbit 10 793, block 169. **(b)** MISR-MODIS reflectance difference image corresponding to **(a)**. The red box indicates where line averaging is done to characterize the left-side background anomaly. **(c)** MISR RGB image for orbit 17 725, block 40. **(d)** MISR-MODIS reflectance difference image corresponding to **(c)**. The purple box indicates where line averaging is done to characterize the right-side background anomaly. **(e)** Average MISR-MODIS reflectance anomaly derived from **(b)** (red line), after first being normalized such that the maximum value would be 1.0 if it were perfectly represented by the fit function. Average MISR-MODIS reflectance anomaly derived from **(d)** (purple line), after first being normalized such that the maximum value would be 1.0 if it were perfectly represented by the fit function.

AMTD
8, 2521–2554, 2015

MISR calibration issues in high-contrast scenes

J. A. Limbacher and R. A. Kahn

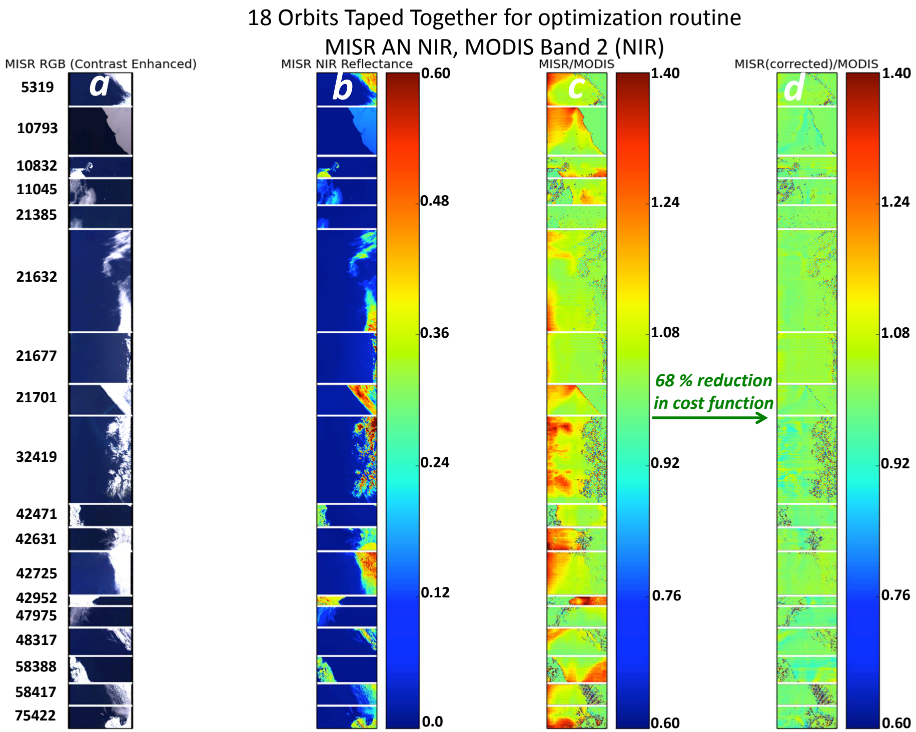

Figure 7. (a) MISR nadir contrast-enhanced RGB images for 18 different scenes, concatenated, and separated by thin white horizontal lines. Numbers to the left indicate Terra orbit. **(b)** MISR nadir NIR reflectance, along with the reflectance color scale. **(c)** MISR-NIR/MODIS-Band 2 reflectance ratios for the images in **(b)** before corrections are applied to the MISR data. The reflectance ratio scale is to the right. **(d)** MISR/MODIS reflectance ratios after the corrections are applied.

AMTD
8, 2521–2554, 2015

MISR calibration issues in high-contrast scenes

J. A. Limbacher and R. A. Kahn

Title Page
Abstract | Introduction
Conclusions | References
Tables | Figures
◀I | ▶I
◀ | ▶
Back | Close
Full Screen / Esc
Printer-friendly Version
Interactive Discussion

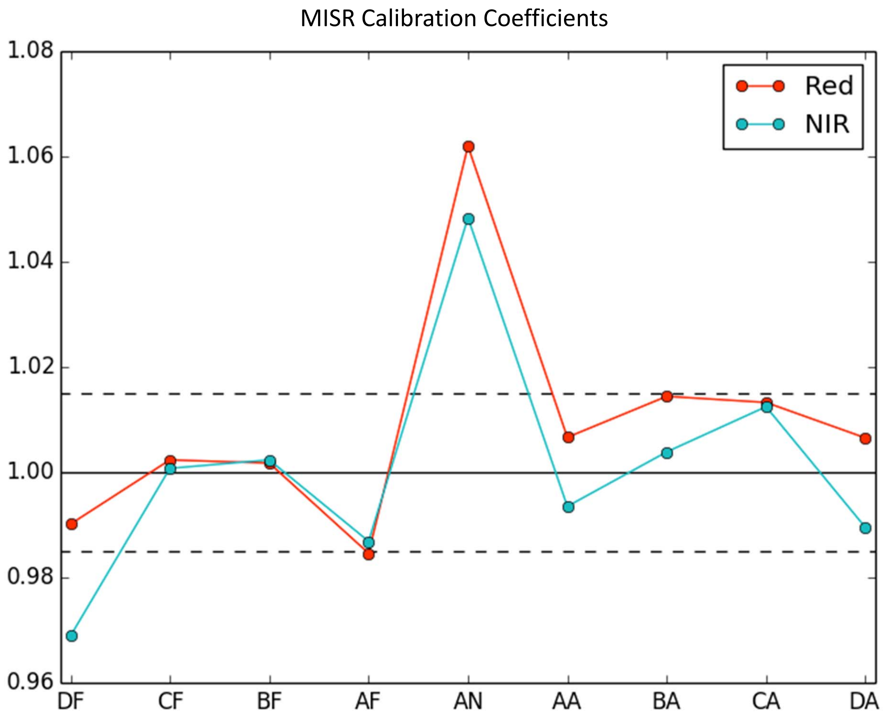

	DF	CF	BF	AF	AN	AA	BA	CA	DA
Red	0.990	1.002	1.002	0.985	1.062	1.007	1.014	1.013	1.007
NIR	0.969	1.001	1.002	0.987	1.048	0.994	1.004	1.012	0.990

Figure 8. Empirical calibration adjustments used to generate the RA + ghosting results shown in Tables 1 and 2. Note that the dotted lines represent ±1.5 %. All the red and NIR channels except the nadir and the NIR for the 70° forward camera fall within these limits. The calibration adjustment numerical values are shown just below the figure. In the plot annotations, "D," "C," "B," and "A" refer to the 70.5, 60, 45.6, 26.1° MISR cameras, respectively, An is the nadir camera, and "f" refers to the forward-viewing and "a" to the aft-viewing cameras.

AMTD
8, 2521–2554, 2015

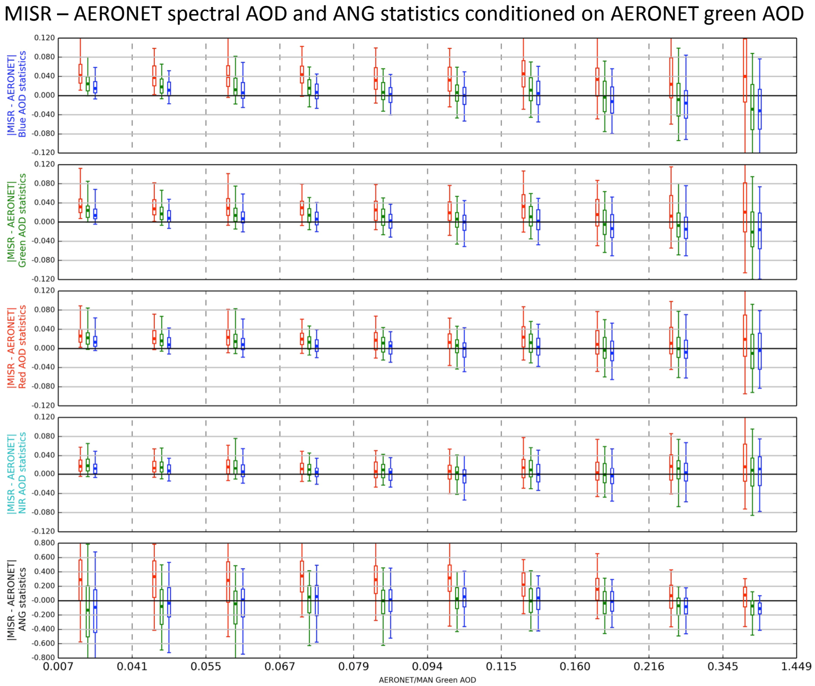

Figure 9. |MISR–AERONET| spectral AOD and ANG statistics conditioned on AERONET mid-visible AOD. For the vertical whiskers and points: red represents the SA, green represents the baseline RA, and blue represents the RA with internal reflection corrections applied. The whiskers indicate the 25–75 %, the lower dot gives the median absolute error, and the upper dot represents the 68 % value. Each row of plots presents results for one of the four MISR spectral bands (blue, green, red, and NIR); the fifth row gives the corresponding results for ANG, assessed between 440 and 867 nm wavelength. Vertical dashed lines separate AOD bins, which are defined based on the AERONET or MAN mid-visible AOD. The upper limit of each mid-visible AOD bin is shown at the bottom of each plot (except for the last AOD bin).

Discussion Paper | Discussion Paper | Discussion Paper | Discussion Paper |

AMTD

8, 2521–2554, 2015

MISR calibration issues in high-contrast scenes

J. A. Limbacher and R. A. Kahn

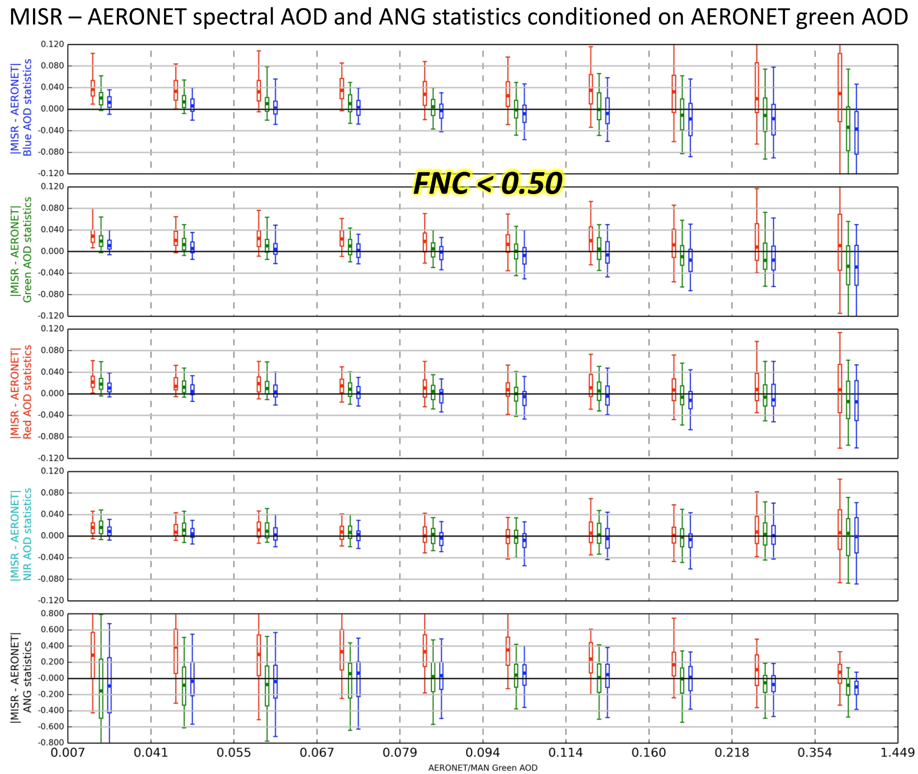

Figure 10. |MISR–AERONET| spectral AOD and ANG statistics conditioned on AERONET mid-visible AOD, with enhanced cloud screening. Same as Fig. 8 except the fraction not-clear (FNC) for the retrieval region must be < 0.5.

Discussion Paper | Discussion Paper | Discussion Paper | Discussion Paper |

AMTD

8, 2521–2554, 2015

MISR calibration issues in high-contrast scenes

J. A. Limbacher and R. A. Kahn